Catalysis Letters 52 (1998) 215–220

On the nature of the active site for the ethylbenzene dehydrogenation over iron oxide catalysts

W. Weiss *, D. Zscherpel and R. Schlögl

Fritz-Haber-Institut der Max-Planck-Gesellschaft, Faradayweg 4-6, 14195 Berlin, Germany
E-mail: weiss_w@fhi-berlin.mpg.de

Received 6 February 1998; accepted 6 April 1998

The dehydrogenation of ethylbenzene to styrene was studied over single-crystalline iron oxide model catalyst films grown epitaxially onto Pt(111) substrates. The role of the iron oxide stoichiometry and of atomic surface defects for the catalytic activity was investigated by preparing single-phased Fe_3O_4(111) and α-Fe_2O_3(0001) films with defined surface structures and varying concentrations of atomic surface defects. The structure and composition of the iron oxide films were controlled by low-energy electron diffraction (LEED) and Auger electron spectroscopy (AES), the surface defect concentrations were determined from the diffuse background intensities in the LEED patterns. These ultrahigh vacuum experiments were combined with batch reactor experiments performed in water–ethylbenzene mixtures with a total gas pressure of 0.6 mbar. No styrene formation is observed on the Fe_3O_4 films. The α-Fe_2O_3 films are catalytically active, and the styrene formation rate increases with increasing surface defect concentration on these films. This reveals atomic surface defects as active sites for the ethylbenzene dehydrogenation over unpromoted α-Fe_2O_3. After 30 min reaction time, the films were deactivated by hydrocarbon surface deposits. The deactivation process was monitored by imaging the surface deposits with a photoelectron emission microscope (PEEM). It starts at extended defects and exhibits a pattern formation after further growth. This indicates that the deactivation is a site-selective process. Post-reaction LEED and AES analysis reveals partly reduced Fe_2O_3 films, which shows that a reduction process takes place during the reaction which also deactivates the Fe_2O_3 films.

Keywords: iron oxide, ethylbenzene dehydrogenation, model catalysis, surface defects

1. Introduction

The catalytic dehydrogenation of ethylbenzene (EB) to styrene is a large-volume synthesis reaction that produces 15 billion pounds product per year worldwide [1]. It is carried out over iron-oxide-based catalysts at temperatures around 870 K in the presence of steam. Technical catalysts contain small amounts of several other metal oxides that act as structural promoters which stabilize the catalyst morphology and prevent sintering of the catalyst pellets. Some of them also increase the selectivity of the catalysts [2,3]. The addition of potassium increases the catalyst activity by at least one order of magnitude and reduces the formation of carbonaceous surface deposits that can deactivate the catalysts [2,4,5]. An active $KFeO_2$ surface phase was first proposed by Hirano [6] and substantiated later by Muhler et al., who studied the working catalyst structure and composition under reaction conditions [7,8]. Very similar apparent activation energies for potassium-promoted and unpromoted iron oxide catalysts were obtained from kinetic studies at pressures in the mbar range. A unimolecular Langmuir–Hinshelwood mechanism with identical active sites for the styrene formation on promoted and unpromoted iron oxide catalysts was proposed [4,6,9]. Potassium only increases the number of active sites, but does not change their nature. The main side products of this reaction, benzene and toluene, are formed at different sites as deduced from the kinetic experiments cited above. Steam reduces the formation of carbonaceous surface deposits that can deactivate the catalyst. It furthermore introduces heat for the endothermic reaction, it prevents a strong reduction of the oxide catalyst, and, as a diluent, it shifts the reaction equilibrium to the product side.

Analogously to the oxidative dehydrogenation of butadiene over $MgFe_2O_4$ catalysts [10], a two-step mechanism associated with an acidic and a basic site is postulated for the dehydrogenation of EB over iron oxide and other transition-metal oxide catalysts [8,11]. The C–H groups of the EB ethyl group get deprotonated at basic oxygen sites, and two hydroxyl groups are formed at the surface. Simultaneously or subsequently, an electron transfer to acidic Fe^{3+} sites is required before the styrene product molecule can desorb from the catalyst surface. Finally, the hydrogen atoms from the two hydroxyl groups must leave the catalyst surface. In the active $KFeO_2$ phase of the technical catalysts, potassium-saturated Fe^{3+}–oxygen bonds create surface oxygen sites with a high basicity, which furthermore must be located in an adequate geometry with respect to the acidic Fe^{3+} sites, so that an effective deprotonation of the EB is possible.

Here we present the first experimental investigation of the styrene synthesis reaction over single-crystalline iron oxide model catalyst samples with defined surface structures and stoichiometries. Since the nature of the active sites is assumed to be identical on promoted and un-

* To whom correspondence should be addressed.

promoted catalysts, we investigate unpromoted iron oxide model catalyst films in a first step. Magnetite $Fe_3O_4(111)$ films 10–50 nm thick were grown epitaxially onto Pt(111) substrates under ultrahigh vacuum (UHV) conditions. They were transformed into α-$Fe_2O_3(0001)$ films by a high-pressure oxidation treatment. STM investigations reveal relatively smooth surface morphologies for these films as well as surface defects like steps, adatoms, surface vacancies and otherwise modified surface atoms [12]. The atomic structure of the $Fe_3O_4(111)$ surface was determined by a dynamical LEED intensity analysis [13]. These structure studies and the electronic film structures, as investigated by several techniques [14,15], demonstrated that the iron oxide films are equivalent to the corresponding bulk oxide samples. Furthermore, no contaminations can be detected with AES and photoelectron spectroscopy, indicating that the films are very clean in contrast, for example, to natural iron oxide single crystals.

In this work, we control the iron oxide phase and, thus, the model catalyst surface structure and stoichiometry with LEED, as discussed more detailed in section 3. From the diffuse background intensities in the LEED pattern, the average surface defect concentrations were deduced. The influence of these factors, surface stoichiometry and atomic surface defects, onto the catalytic activities of the model catalyst films was investigated. For this the surface structure characterization in UHV was combined with *in situ* batch reactor experiments at total gas pressures of 0.6 mbar.

2. Experimental

The experiments were performed in a three-chamber UHV surface analysis system with a newly designed sample transfer mechanism, which is desribed in detail in [16]. The central chamber of this system was used for sample preparation in ambient gas pressures up to 10^{-6} mbar. It had a base pressure of 1×10^{-10} mbar and was equipped with a quadrupole mass spectrometer (QMS) for performing thermal desorption spectroscopy (TDS) and temperature-programmed reaction (TPR) experiments, a backview LEED optics and a cylindrical mirror analyzer for AES. The full width at half maximum (FWHM) of the LEED spots and the diffuse background intensities were determined from diffraction intensity line scans. The platinum crystal can be heated resistively with two tungsten wires and by electron bombardment from the back. The sample temperature is measured with a cromel–alumel thermocouple spotwelded to the side of the crystal.

A high-pressure reaction cell made from a 64 mm double cross is attached to this central chamber. It has a base pressure of 1×10^{-9} mbar and can be completely seperated from the central chamber by a 64 mm gate valve after the sample transfer. It is used for high-pressure oxidation treatments and for the batch reactor experiments. The sample is placed into a heating station equipped with sprung electrical feedthrough contacts that provide resistive heating and thermocouple temperature control [16]. EB and water were dosed with leak valves into the batch reactor, establishing a 1 : 10 molar ratio at a total gas pressure of 0.6 mbar. The reactant and product concentrations were detected with the QMS in the central chamber, which was connected via a capillar to the batch reactor. All QMS signals were corrected by signals that result from thermal cracking of larger molecules at the QMS filament.

The PEEM measurements were performed in a second analysis chamber, which also is connected to the central TDS chamber from which it can be separated by a 64 mm gate valve. It also has a base pressure of 1×10^{-10} mbar. The sample is illuminated with a mercury discharge lamp located outside this chamber, and the PEEM image is monitored from the fluorescent screen with a video camera connected to a personal computer.

The platinum substrate surface was prepared by repeated cycles of Ar^+ ion bombardment (1 keV, 2 μA) and annealing to 1300 K, until a sharp Pt(111) LEED pattern and no AES contamination signals were observed anymore. Well ordered $Fe_3O_4(111)$ films were grown onto the Pt(111) surface by repeated cycles of iron deposition at room temperature and subsequent oxidation at about 900 K in 10^{-6} mbar oxygen partial pressure. The Fe_3O_4 films were transformed into well ordered α-$Fe_2O_3(0001)$ films by an oxidation treatment at 900 K in 0.1 mbar oxygen partial pressure. The precise growth mode and surface morphologies of these films depend on the exact preparation conditions, as described in detail in [12].

3. Results and discussion

3.1. Model catalyst film structures and stoichiometries

Fe_3O_4 (magnetite) crystallizes in the cubic inverse spinel structure, where the oxygen anions form a close packed fcc lattice with Fe^{2+} and Fe^{3+} cations occupying the tetrahedral and octahedral interstitials. α-Fe_2O_3 (hematite) crystallizes in the hexagonal corundum structure, where the oxygen anions form a close packed hcp lattice with Fe^{3+} occupying only octahedral interstitials. Figure 1(a) displays a top view onto the unreconstructed hexagonal surfaces of Fe_3O_4 and α-Fe_2O_3 with a topmost iron layer. The iron sublattices in these two oxide structures create the two different hexagonal surface unit cells indicated by the solid lines. On $Fe_3O_4(111)$, the unit cell vectors are 6 Å long, on α-$Fe_2O_3(0001)$, they are 5 Å long and rotated by 30° against those on $Fe_3O_4(111)$. Figure 1(b) shows the LEED patterns we observe on these films. They correspond to unreconstructed $Fe_3O_4(111)$ and $Fe_2O_3(0001)$ surface terminations with the two surface unit cells displayed in figure 1(a). These LEED patterns allow us to identify the two iron oxide phases. They further show that single-phased films were prepared, whereas films consisting of both oxide phases exhibit a superposition of the two LEED patterns shown in figure 1(b).

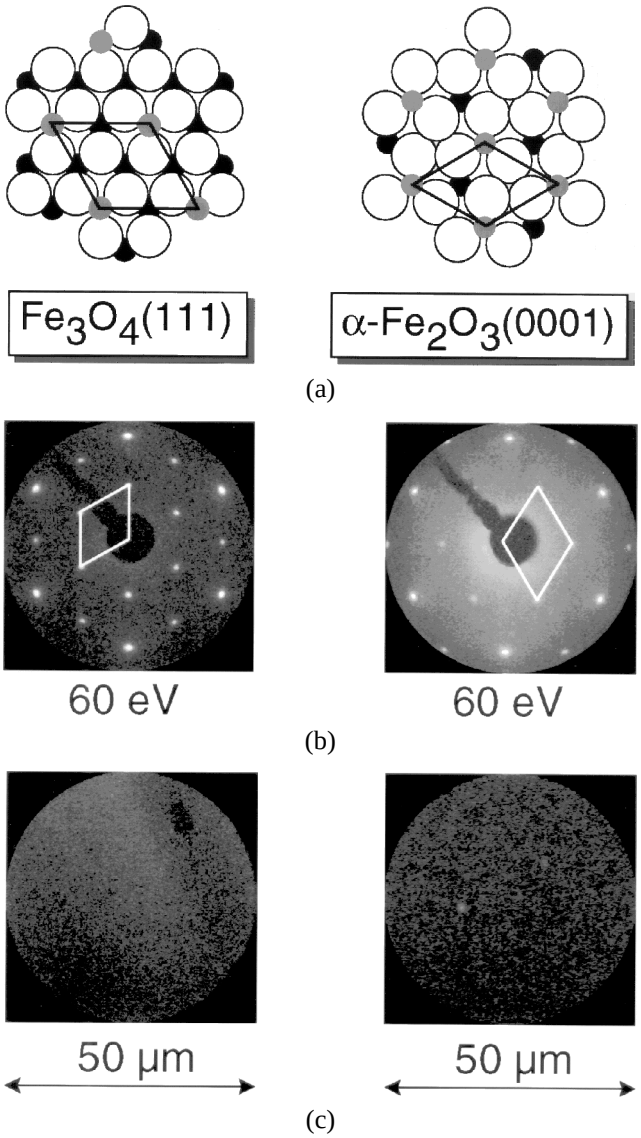

Figure 1. (a) Top view onto the unreconstructed hexagonal surfaces of Fe_3O_4 and α-Fe_2O_3 with iron atoms in the topmost layer (small grey circles). Second-layer oxygen atoms are displayed as large white circles, and third-layer iron atoms as small black circles. The surface unit cells are indicated. (b) LEED pattern of $Fe_3O_4(111)$ and α-$Fe_2O_3(0001)$ films grown epitaxially onto Pt(111), taken at 60 eV electron energy. The reciprocal unit cells are indicated. (c) 50 μm diameter PEEM images of the clean iron oxide films indicated in (a).

The atomic structure of the $Fe_3O_4(111)$ surface was determined in a previous LEED intensity analysis [13]. It forms an unreconstructed termination, as shown in figure 1(a), with $1/4$ monolayer iron in the topmost layer as well as strong interlayer relaxations in the surface region. A determination of the α-$Fe_2O_3(0001)$ surface structure is underway. As known from STM measurements, the surface roughness of the oxide films depends on the exact preparation procedure and ranges between 40 and 300 Å on a length scale of 1 μm, the film thickness is at least 100 Å [12]. On the $Fe_3O_4(111)$ films we observe atomic steps mostly with a height of 4.5 Å and some steps with multiple heights thereof, which correspond to the distance between equivalent terminations of $Fe_3O_4(111)$. On the α-$Fe_2O_3(0001)$ films we observe monoatomic steps 2.5 Å high and some multiatomic steps. With increasing step density, the FWHM of the LEED spots increases for electron energies corresponding to out-of-phase scattering conditions [17]. We also observe point defects in our STM images, which can be attributed to vacancies, adatoms or otherwise modified surface atoms [12]. Point defects create a uniform background intensity inbetween the LEED spots if they are randomly distributed on the surface. The background intensity increases with increasing point defect density on the surface [17]. In this work, we did not determine absolute numbers of steps and point defects, since this requires the knowledge of the point defect scattering factors and the measurement of electron-energy-dependent FWHM. Instead, we compared the defect densities that have formed on the different oxide films.

The PEEM images we observe on these clean oxide films are shown in figure 1(c). They display surface regions with a diameter of 50 μm. No features are visible which indicates that no structures larger than the lateral resolution of the microscope (300 nm) exist on the clean model catalyst film surfaces.

The stoichiometry and cleanliness of the two iron oxide films is demonstrated by AES and X-ray photoelectron spectroscopy measurements (not shown here), where no contamination signals were detected. The intensity ratio between the O(KLL) and Fe(LMM) signals are 3.1 for the Fe_3O_4 and 3.9 for the Fe_2O_3 AES spectra, which approximate the stoichiometries of these two oxide phases when considering the cross sections of the corresponding Auger electrons [18]. X-ray photoelectron spectroscopy measurements revealed the characteristic Fe 2p core level binding energies and satellite emission features for Fe^{2+} and Fe^{3+} in these two oxide films, demonstrating their equivalence to the corresponding bulk oxides [14].

3.2. Reactivity studies

On the left side of figure 2, the LEED patterns of three $Fe_2O_3(0001)$ films are shown before the reaction experiments were performed. The diffuse background intensities in these LEED patterns were quantified by the ratio between the maximal intensity $I_{\max}$ of the (10) LEED spot indicated by the arrows and the background intensity I_B measured inbetween the main diffraction spots. The FWHM of the (10) beam is quantified in percent of the first Brillouin zone width given by the $Fe_2O_3(0001)$ surface unit cell indicated in figure 1. Since the electron energy $E = 60$ eV corresponds to an intermediate scattering condition, this FWHM scales with the step densities on the surfaces. Film 1 has the lowest step and point defect density on the surface, film 2 has a medium and film 3 has the highest step and point defect density, as indicated by the numbers below the LEED patterns. On the left side of figure 3, the LEED patterns of two Fe_3O_4 films are shown. Film 1 has a low density and film 2 a higher density of surface steps and point defects.

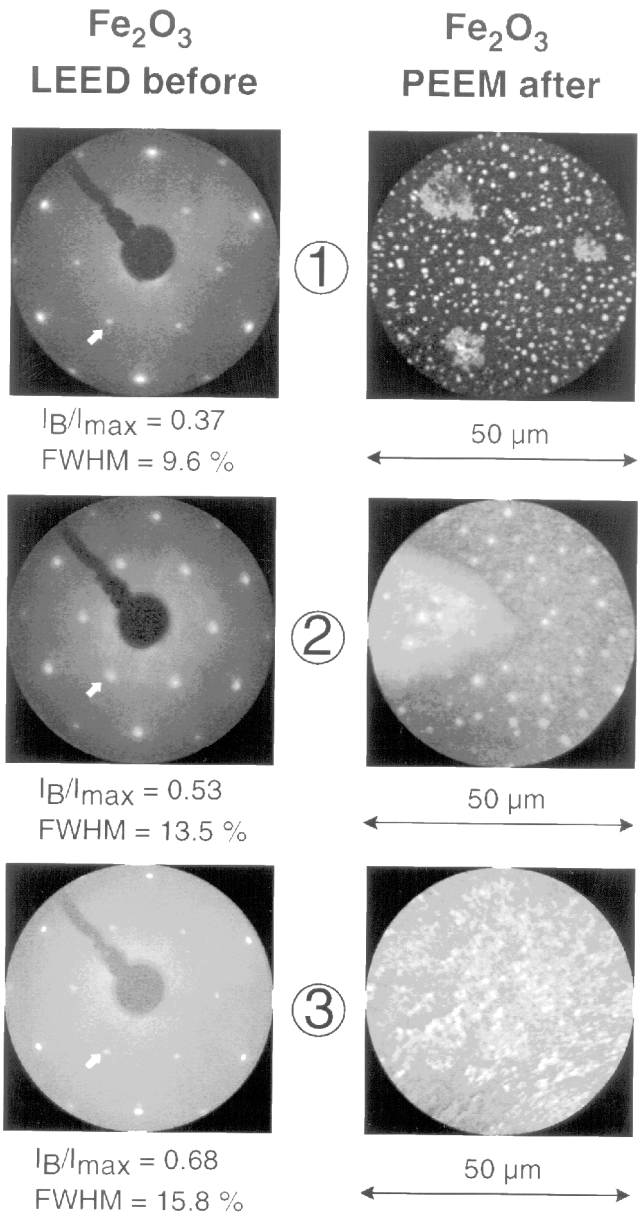

Figure 2. On the left-hand side, the LEED patterns of three $Fe_2O_3(0001)$ films taken at $E = 60$ eV before the reaction experiments are shown. Below the LEED patterns, the full width at half maximum (FWHM) of the (10) beams indicated by the arrows are given, as well as the ratios between the diffuse background intensities I_B and the maximal intensities of the (10) beams I_{max}. Film 1 has a low step and point defect density on the surface, film 2 a medium and film 3 a high step and point defect density. On the right-hand side, the 50 μm diameter PEEM images observed on the three films after the reaction experiments are shown.

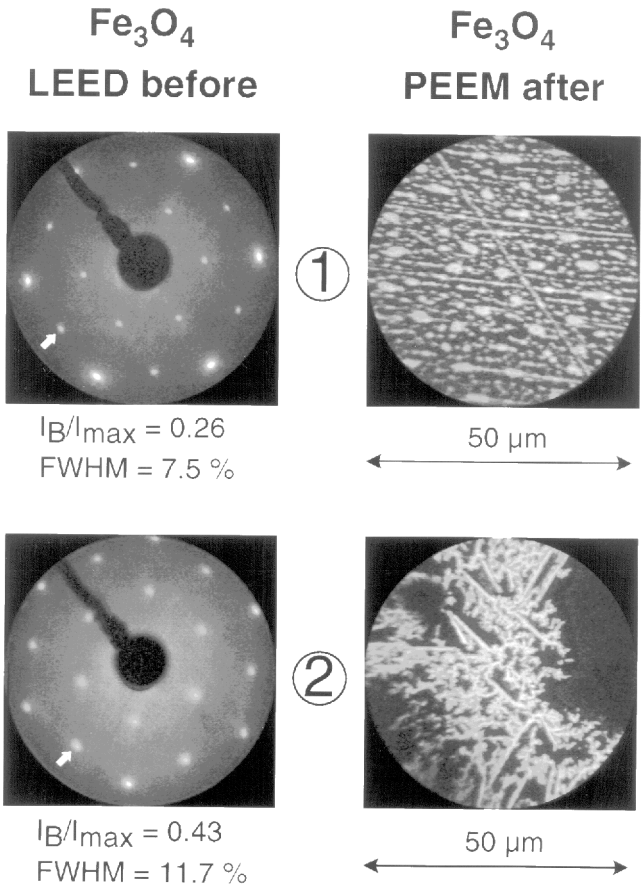

Figure 3. On the left-hand side, the LEED patterns of two $Fe_3O_4(111)$ films taken at $E = 60$ eV before the reaction experiment are shown. On the right-hand side, 50 μm diameter PEEM images observed after the reaction experiment are shown. Analogously to figure 2, the FWHM and the background intensities are indicated below the LEED patterns. Fe_3O_4 film 1 has a low step and point defect density, and film 2 has a higher step and point defect density on the surface.

Figure 4 displays the results of the batch reactor experiments performed on these model catalyst films. After admission of the educts, the samples were heated from room temperature up to the reaction temperature of 870 K, which was reached after 12 and 7 min, as indicated by the arrows. For the low defect density Fe_2O_3 film 1 in figure 4(a), no significant changes in the EB and styrene signals are observed, indicating no catalytic styrene formation. Only a small increase of the hydrogen signal can be seen. On the medium defect density film 2 and on the high defect density film 3, stronger hydrogen and styrene formations are observed, accompanied by simultaneous decreases of the EB concentrations in the batch reactor. With increasing surface defect concentrations on the Fe_2O_3 model catalyst films, the formation rates of the reaction products styrene and hydrogen increase, accompanied by an increasing consumption of the EB reactant in the batch reactor. After about 30 min reaction time, the active films 2 and 3 get deactivated, and the styrene and hydrogen product concentrations do not increase considerably with time anymore. Figure 4(b) displays the reaction experiments performed on the Fe_3O_4 films. Independent on the surface defect concentrations, no catalytic styrene formation is observed on these films, no hydrogen evolution and no significant decrease of the EB concentration in the batch reactor. These experiments clearly reveal atomic surface defects as active sites for the dehydrogenation of EB to styrene on the α-$Fe_2O_3(0001)$ model catalyst films, whereas the Fe_3O_4 phase is not catalytically active.

After the reaction experiments, the model catalyst films are covered with carbonaceous surface deposits. The AES spectra of these deposits (not shown here) look graphitic

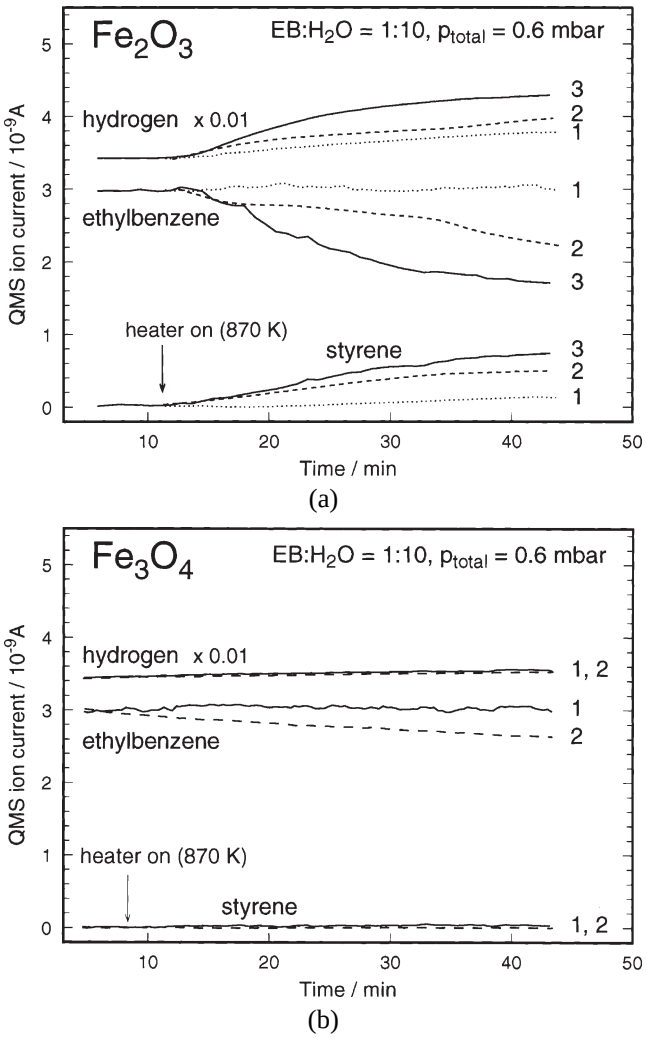

Figure 4. (a) Batch reactor experiments on epitaxial Fe_2O_3(0001) films with a low (1), medium (2) and high surface defect density (3). A mixture of ethylbenzene and water with a molar ratio of 1 : 10 and a total pressure of 0.6 mbar was established. The QMS intensities for the molecular masses of hydrogen, EB and styrene are displayed as a function of time. An offset was added to the hydrogen signal for better presentation. (b) Batch reactor experiments on epitaxial Fe_3O_4(111) films with a low (1) and higher surface defect density (2).

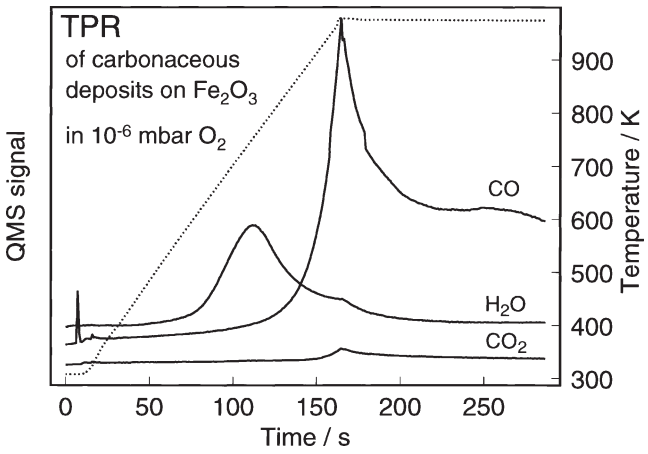

Figure 5. Temperature-programmed reaction experiment in the presence of 10^{-6} mbar oxygen, performed on the most active Fe_2O_3 film 3 covered by a hydrocarbon layer after the reaction experiment. The QMS signals for the molecular masses of CO, H_2O and CO_2 are shown as a function of time. The dotted line indicates the sample temperature which is given on the right side.

with respect to their energetic positions and line shapes. In figure 5, a typical TPR experiment performed after the reaction experiment is shown. The Fe_2O_3 film 3 was transferred back into the TDS chamber and heated up to 1000 K in 10^{-6} mbar oxygen partial pressure. The dotted line indicates the temperature evolution. First the desorption of water is observed, followed by desorption of CO and some CO_2. The similar amounts of detected water and CO indicate the combustion of hydrocarbon molecules that have formed on the film during the batch reactor experiments.

The hydrocarbon surface deposits were imaged with the PEEM microscope. On the low defect density Fe_2O_3 film 1 in figure 2, bright dots about 1 μm in size are randomly distributed on the surface. The regions inbetween these bright dots exhibit the same contrast as the clean oxide films in figure 1. Therefore we attribute the dark areas to clean Fe_2O_3 surface regions and the bright dots to carbonaceous surface deposits. Film 2 with a medium defect density also exhibits bright dots randomly distributed on the surface, but now the region inbetween these bright spots is considerably brighter, when compared to film 1. As all PEEM images were measured under identical experimental conditions, we conclude that the regions inbetween the bright spots on film 2 also are covered with carbonaceous surface deposits. The most active Fe_2O_3 film 3 is covered by a thick hydrocarbon layer after the reaction experiment, as evident from its PEEM image with the highest brightness. This indicates that the formation of carbonaceous deposits is correlated to the catalytic film activity. It deactivates films 2 and 3 after about 30 min, when the surfaces are completely covered by the hydrocarbon layers. Like on the Fe_2O_3 film 1 with a low defect density, small amounts of carbonaceous surface deposits also are observed on both Fe_3O_4 films after the reaction experiments, although no gaseous product formation was detectable on these films. As can be seen on the right side of figure 3, these deposits form dots and some streaky features on film 1, whereas dentritic-like structures were formed on film 2 which had a higher surface defect density. These dentritic structures indicate a polymerization of the hydrocarbon deposits.

The PEEM measurements monitor the deactivation process on the model catalyst films caused by carbonaceous surface deposits. This process presumably starts at mesoscopic defect sites which have different properties than the catalytically active atomic defect sites. They exist both on the active Fe_2O_3 and on the inactive Fe_3O_4 films. The further growth of the surface deposits seems to be related to the catalytic film activities, as the inactive Fe_3O_4 films are not covered completely after the reaction experiments by them, whereas on the Fe_2O_3 films the deposit coverage increases with increasing catalytic activity. After the reaction experiments, the Fe_2O_3 films are partly reduced

to Fe_3O_4, as observed with LEED after removing the deposits by combustion, as shown in figure 5. This indicates that a reduction process takes place during the reaction experiments which also contributes to the deactivation of the Fe_2O_3 films.

4. Summary and conclusions

The catalytic dehydrogenation of ethylbenzene to styrene in the presence of steam was investigated over single-crystalline iron oxide model catalyst films with defined surface structures and stoichiometries. No styrene formation is observed on the Fe_3O_4(111) films, whereas on Fe_2O_3(0001) films the styrene formation increases with increasing surface defect concentration. This clearly reveals atomic surface defects as catalytically active sites on unpromoted α-Fe_2O_3(0001) films, which is the active iron oxide phase for this reaction. The local geometry of the active sites must be given by steps, vacancies, adatoms or isolated surface atoms with a modified local electronic structure. All these types of defects have been observed in recent STM investigations on these model catalyst films. Most likely, oxygen anions with a higher basicity are exposed at these defect sites, which effectively can deprotonate the C–H groups of the ethyl group of the EB molecule. Simultaneously or subsequently to this deprotonation, an electron must be transferred from the reaction intermediate to an acidic Fe^{3+} site. This is one reason for Fe_3O_4 not being active, because less Fe^{3+} species exist in this phase when compared to Fe_2O_3. At atomic defect sites on the α-Fe_2O_3(0001) surface, a more favorable geometric arrangement of the basic and acidic sites might be established, which is an important factor for their effective action in an almost simultaneous manner. The similar apparent activation energies observed on unpromoted and potassium-promoted iron oxide catalysts indicate an identical nature of the active sites thereon [4,9]. Therefore, the active sites on the $KFeO_2$ surface phase of the technical catalysts must have similar properties as atomic defects on the Fe_2O_3(0001) surface.

The present experiments have shown for the first time that on single-crystalline model oxide films catalytic processes can be studied under conditions approximating the real situation. The active surface phase structure and the crucial role of atomic surface defects on reactivity were highlighted. The catalyst deactivation by formation of carbonaceous polymers was identified to be a site-selective process by observing patterning of the deactivated surface areas with the PEEM. It seems likely that the inital carbon formation takes place at extended defects, which are not identical to the atomic defects of the styrene formation. The further growth of the carbonaceous deposits is clearly correlated to the film activities, after prolonged batch reactor operation the active catalysts are overgrown with deposits. Potassium promotion and the use of an atmospheric pressure flow reactor will enable us to complete these studies under even more realistic conditions by maintaining the pre- and post-reaction control of surface structure and stoichiometry.

Acknowledgement

We thank Manfred Swoboda for his excellent technical assistance.

References

[1] K. Kochloefl, in: *Handbook of Heterogeneous Catalysis*, Vol. 5, eds. G. Ertl, H. Knözinger and J. Weitkamp (Wiley–VCH, 1997) p. 2151.
[2] E.H. Lee, Catal. Rev. 8 (1973) 285.
[3] A.K. Vijh, J. Chim. Phys. 72 (1975) 5.
[4] T. Hirano, Appl. Catal. 26 (1986) 65.
[5] K. Coulter, D.W. Goodman and R.G. More, Catal. Lett. 31 (1995) 1.
[6] T. Hirano, Appl. Catal. 28 (1986) 119.
[7] M. Muhler, J. Schütze, M. Wesemann, T. Rayment, A. Dent, R. Schlögl and G. Ertl, J. Catal. 126 (1990) 339.
[8] M. Muhler, R. Schlögl and G. Ertl, J. Catal. 138 (1992) 413.
[9] W.P. Addiego, C.A. Estrada, D.W. Goodman, M.P. Rosynek and R.G. Windham, J. Catal. 146 (1994) 407.
[10] M.A. Gibson and J.W. Hightower, J. Catal. 41 (1976) 420.
[11] I. Wang, J.-C. Wu and C.-S. Chung, Appl. Catal. 16 (1985) 89.
[12] M. Ritter, W. Weiss and R. Schlögl, to be published.
[13] W. Weiss, A. Barbieri, M.A. Van Hove and G.A. Somorjai, Phys. Rev. Lett. 71 (1993) 1848.
[14] Th. Schedel-Niedrig, W. Weiss and R. Schlögl, Phys. Rev. B 52 (1995) 17449.
[15] Y.Q. Cai, M. Ritter, W. Weiss and A.M. Bradshaw, Phys. Rev. B (1998), in press.
[16] W. Weiss, M. Ritter, D. Zscherpel, M. Swoboda and R. Schlögl, J. Vac. Sci. Technol. A 16 (1998) 21.
[17] M. Henzler, in: *Electron Spectroscopy for Surface Analysis*, ed. H. Ibach (Springer, Berlin, 1979).
[18] P.W. Palmberg, G.E. Riach, R.E. Weber and N.C. MacDonald, *Handbook of Auger Electron Spectroscopy* (Physical Electronics Industries, Inc., Eden Prairie, MN, 1972).
[19] M.P. Seah and W.A. Dench, Surf. Interface Anal. 1(1) (1979) 2.